Contents lists available at ScienceDirect

Materialia

journal homepage: www.elsevier.com/locate/mtla

Full Length Article

THE influence of copper addition on crack initiation and propagation in an Al–Si–Mg alloy during cyclic testing

Toni Bogdanoff [a],[*], Lucia Lattanzi [b], Mattia Merlin [b], Ehsan Ghassemali [a], Salem Seifeddine [a]

[a] Department of Materials and Manufacturing, Jönköping University, Box 1026, 55111 Jönköping, Sweden
[b] Department of Engineering, University of Ferrara, Via Giuseppe Saragat 1, 44122 Ferrara, Italy

A B S T R A C T

The effect of copper (Cu) addition up to 3.2 wt% on crack initiation and propagation in an Al–Si–Mg cast alloy was investigated using *in-situ* cyclic testing in the as-cast condition. A combination of digital image correlation, electron backscatter diffraction, and scanning electron microscopy was used to investigate crack initiation and propagation behaviour during *in-situ* cyclic testing. The results showed that Cu-rich intermetallic compounds with the addition of Cu up to 1.5 wt% do not affect the fatigue behaviour of these alloys, and that crack propagation in these cases is trans-granular and trans-dendritic. However, increasing the concentration of the Cu retained in the primary α-Al matrix in solid solution and Cu-containing precipitates delayed crack propagation during cyclic testing. The results showed that strain accumulation was highest at the grain boundaries; however, the crack preferred to propagate along or across primary α-Al dendrites due to the relatively lower mechanical strength of the matrix compared to the eutectic and intermetallic phases. Moreover, the addition of Cu of more than 3.0 wt% to Al-Si-Mg alloys changes the fatigue behaviour that a rapid failure occurs.

1. Introduction

It is of interest to the automotive industry to combine the ductility of alloy A356 (Al–7Si–Mg) and the tensile properties of alloy A319 (Al–6Si–Cu). Therefore, focusing on the microstructure is fundamental to assess the desired mechanical properties. The addition of small amounts of copper (Cu) to A356 could be one way of obtaining a microstructure that combines the properties of both A356 and A319. At the same time, it is crucial to attaining a composition that minimises the formation of Cu-related hot tearing and shrinkage porosity [1–3].

Cu additions to Al–Si–Mg cast alloys have been extensively investigated over the last two decades, as this leads to increased tensile mechanical properties due to solid-solution and precipitation strengthening. Cu changes the precipitation sequence and thus improves the strengthening phases of an Al–Si–Mg system. Besides β-Mg$_2$Si, Q-Al$_5$Mg$_8$Cu$_2$Si$_6$ begins to precipitate when Cu is present in such alloys. For Cu contents of above 1 wt%, magnesium (Mg) is involved only in the Q phase, and the precipitation of the θ-Al$_2$Cu phase occurs.

Several studies of as-cast Al–Si–Mg alloys to which Cu was added investigated the influence of melt quality, porosity, and Cu intermetallic phases on tensile properties [4–8]. The results showed discrepancies due to the fact that the increases in yield strength (YS) and ultimate tensile strength (UTS) were not of similar magnitude for the same

Cu contents. It is worth noting that these results are not directly comparable, as microstructural features such as secondary dendrite arm spacing (SDAS) and average grain size (AGS) were not clearly stated. Besides, the alloy conditions, such as grain refining and Sr modification, were not similar. Taghiabadi et al. [4] reported a maximum increase in UTS of 30% with the addition of 1.5 wt% of Cu; at the same time, elongation showed a continuous decrease with increasing Cu content. Shabestari and Moemeni [5] observed a maximum increase of 23% for YS and 6% for UTS with a Cu content of 1.5 wt%, with different cooling rates, while elongation continuously decreased with increasing Cu content. The same authors reported that the effect of Cu on porosity formation decreased with higher cooling rates. Both studies conclude that shrinkage porosity becomes significant when the Cu content is higher than 1.5 wt%, and at that point outweighs the beneficial effects of Cu-based compounds on alloys tensile properties. For this reason, the maximum increase in tensile properties was observed for the addition of 1.5 wt% of Cu content. Seifeddine et al. [6] investigated both Cu additions in a wide range (from 0.6 to 5.4 wt%) and solidification rates, with SDAS ranging from 10 to 50 μm. The authors obtained a continuous increase in UTS for each SDAS value: specifically from 20% to 60% with SDAS 10 μm, from 20% to 30% with SDAS 25 μm, and from 12% to 44% with SDAS 50 μm. In addition, elongation showed a decreasing trend with an increase in Cu content. As the investigated

Table 1
Nominal chemical composition [wt%] and the density of the investigated alloys. Error is the standard error.

Alloy	Si	Mg	Cu	Fe	Ti	Sr	Al	Density [g/cm³]	Theoretical density [g/cm³]
Cu 0	6.80	0.38	0.00	0.10	0.07	0.03	Balance	2.65 ± 0.003	2.67
Cu 0.5	7.01	0.37	0.51	0.09	0.07	0.02	Balance	2.66 ± 0.004	2.68
Cu 1.5	7.14	0.38	1.61	0.09	0.07	0.02	Balance	2.68 ± 0.004	2.71
Cu 3.0	6.98	0.36	3.23	0.17	0.08	0.02	Balance	2.70 ± 0.008	2.74

specimens were directionally solidified, the mechanical properties were beneficially influenced by Cu contents of greater than 1.5 wt%. Di Giovanni et al. [7] observed an increase in the range of 25–30% for UTS with 1 wt% of Cu content, for SDAS going from 30 to 40 μm.

To the knowledge of the authors, limited attention has been paid to the crack initiation and crack propagation of as-cast Al–Si–Mg alloys as a result of the addition of Cu. Furthermore, interactions between microstructural features such as α-Al matrix, morphology and distribution of eutectic Si particles, and Cu phases need to be assessed. The influence of Cu, involved either in intermetallic compounds or promoting shrinkage porosity, on tensile properties has been the focus of some studies [3–6]. However, little attention has been paid to the influence of Cu in solid-solution and Cu-based phases on crack nucleation and propagation in cyclic testing. A deep understanding of the link between cracking behaviour and as-cast microstructure is necessary for adequately designing components in terms of alloy selection and heat-treatment. Notably, the increasing demand from the automotive industries for such alloys highlights the importance of such studies. The initiation and growth of microstructural short cracks depend significantly on the microstructure and results from interrupted fatigue testing, and investigation of fracture surfaces provides information about crack initiation and propagation [9–10]. This work investigates the effect of the α-Al matrix, Al-Si eutectic, intermetallic phases, grain size, and stress concentration during *in-situ* cyclic testing, providing novel information regarding crack initiation and propagation in an Al–Si–Mg alloy with varying Cu contents.

This paper presents the results of cyclic tests performed on Al-Si-Mg alloys with the addition of Cu up to 3.2 wt%, and the work described aims to identify the microstructural features that have the most significant effect on crack initiation and propagation.

2. Experimental procedure

Pure Al ingots, pure Si, and an Al–50Mg master alloy were melted in a boron nitride-coated crucible to prepare four Al–Si–Mg alloys with different Cu concentrations. Cu contents were obtained with the addition of an Al–50Cu master alloy. After the completion of melting, grain refiner (Al–5Ti–1B) and modifier (Al–10Sr) master alloys were also added in order to achieve the intended contents of 650–700 ppm of titanium (Ti) and 200–250 ppm of strontium (Sr). Table 1 presents both the name and chemical composition of each alloy, and the latter evaluated using a Spectromaxx CCD LMXM3 optical emission spectrometer (OES).

Cylindrical rods with a length of 150 mm and a diameter of 9 mm were cast in a pre-heated graphite-coated permanent mould. The rods were re-melted at 730 °C for 30 min in an inert gas atmosphere, then drawn from a directional solidification furnace raising at ~6 mm/s, leading to an intended average SDAS of 10 μm and AGS of 90 μm. Tensile testing specimens with a gauge length of 36 mm and diameter of 6 mm were machined from the directionally solidified samples (Fig. 1a). Testing was carried out at room temperature following the ASTM E8 standard with a constant crosshead speed of 0.5 mm/min, and a minimum of three samples was tested for each Cu concentration. A clip-on extensometer was used to measure the strain. Miniature compact-tension (CT) samples were cut using the electron discharge machining method and a 0.25 mm wire. The dimensions of the miniature CT sample, shown in Fig. 1b, were designed according to the ASTM E647-00 Standard.

The samples were ground and mechanically polished with diamond suspension up to 1 μm followed by 0.05 μm colloidal silica. The samples
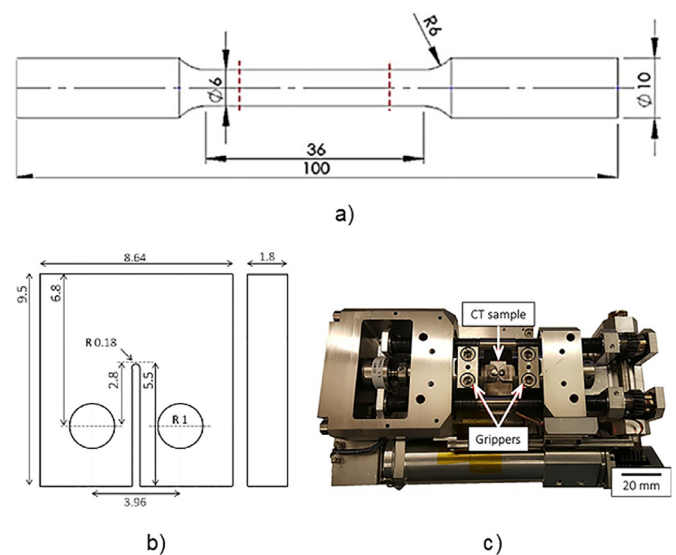
Fig. 1. a) dimensions of the tensile sample in mm; b) dimensions of the CT sample in mm; c) miniature stage for *in-situ* cyclic tests.

were then slightly etched with a 10% NaOH solution to maintain a sufficient level of contrast between the surface and the Si particles after digital image correlation (DIC) pattern generation. Electron backscatter diffraction (EBSD) maps were acquired before and after the *in-situ* cyclic tests in order to investigate the interactions between crack paths and grain boundaries. Wavelength-dispersive X-ray spectroscopy (WDS) was used to measure the Cu content in the primary α-Al matrix, both in the centre and at the edge of the dendrite, while energy-dispersive X-ray spectroscopy (EDS) was employed to identify the various Cu phases. The Thermo-Calc simulation, performed using the Scheil calculator, enabled solidification sequences and the number of different phases in the investigated alloys to be predicted.

In-situ cyclic testing was performed on a Kammrath and Weiss stage (Fig. 1c) in a TESCAN Lyra3 scanning electron microscope (SEM) at room temperature. Before cyclic loading, monotonic tension loading to failure showed that the crack initiated at the notch, at a critical stress intensity factor, K_c, equal to 21 ± 0.4 MPa•$\sqrt{m}$ in all of the alloys. To the knowledge of the authors, the ΔK threshold values for the investigated alloys in an as-cast condition are not available in the literature. Available data report a ΔK threshold range of 3.3–5.1 MPa•$\sqrt{m}$ for unmodified and Sr-modified A356 and A319 alloys in T4, T61, and T71 heat-treated conditions [11]. The miniature samples in this investigation could not be directly compared to the other work because of a possible scale effect. In light of this, the selected $\Delta K = (1 - R)•K_{max}$ value was equal to 12 MPa•$\sqrt{m}$, with a load ratio, R, of 0.2 and K_{max} of 15 MPa•$\sqrt{m}$. A preload 20% higher than was selected pre-crack the samples. The speed of loading was set to 10 μm/s (~0.1 Hz). A minimum of 2 samples of each alloy was tested, and all of the samples survived at least 300 cycles. Focused ion beam (FIB) milling was used to produce a random speckle pattern for DIC analysis, according to the method proposed and validated by Kasvayee et al. [12]. It was beforehand verified that the patterns did not affect the propagation paths of cracks (Fig. 2).
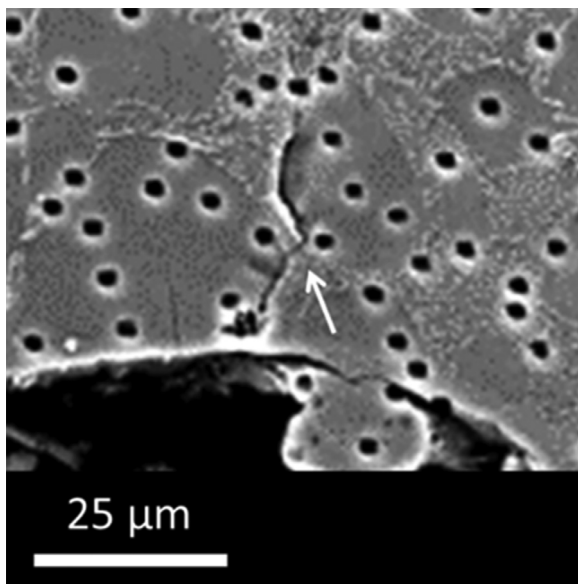
Fig. 2. Detail of crack propagation that is independent of the pattern.

Table 2
Correlation parameters used for 2D DIC analysis.

Pixel size [μm]	0.24
SS = Subset size [pixel]	61
ST = Step size [pixel]	8
Correlation criterion	Zero–normalised sum of squared differences
Shape function	Quadratic
Interpolation function	Bi-cubic polynomial
Displacement standard deviation [pixel]	0.1
SW = Strain window size [pixel]	15
SSR = Strain spatial resolution [pixel]	173 (42 μm)
SSR = SS + [(SW- 1) • ST]	

Fig. 3. a) SEM image of Alloy Cu 3.0: eutectic Si and Cu phases; b) related EDS spectra.

DIC was performed using the MatchID software to obtain strain distribution on the micrographs captured at different cycles. Table 2 presents the correlation parameters used for the DIC analysis.

The field of view (FOV) was 300×300 μm^2 and included the notch tip, in order to investigate local strain development. Moreover, in order to understand the influence of Cu on the α-Al matrix, nanoindentation tests (100 for each sample) were performed using a Micro Materials NanoTest Vantage instrument at a load of 10 mN.

3. Results and discussion

3.1. Microstructural and mechanical properties

The main findings of the investigation of the alloy microstructures are presented in Table 3.

The average SDAS of 9 ± 0.7 μm corresponds to a cooling rate (CR) of 42.8 °C/s according to the relation CR = $2 \cdot 10^4 \cdot (SDAS)^{-2.67}$, proposed by Samuel and Samuel for aluminium foundry alloys [13]. The average grain size of the alloys was 90 ± 2 μm, confirming that the four alloys were in the same grain-refining condition. Similarly, the Sr modification of the alloys led to the formation of Si particles with comparable values of dimensional and geometrical parameters. Table 3 lists the values of the Si particle area and equivalent diameter ED = $(4 \cdot area/\pi)^{1/2}$ varying in the ranges of 0.4–0.5 μm^2 and 0.2–0.3 μm, respectively. The values of aspect ratio (Feret$_{min}$/ Feret$_{max}$) and circularity ($4 \cdot \pi \cdot area/perimeter^2$), as defined by the ISO 9276-6:2008 standard, further confirm that a homogenous morphology of the Si particles is present and is reasonably close to the circular one. Table 4 reports the WDS measurements of
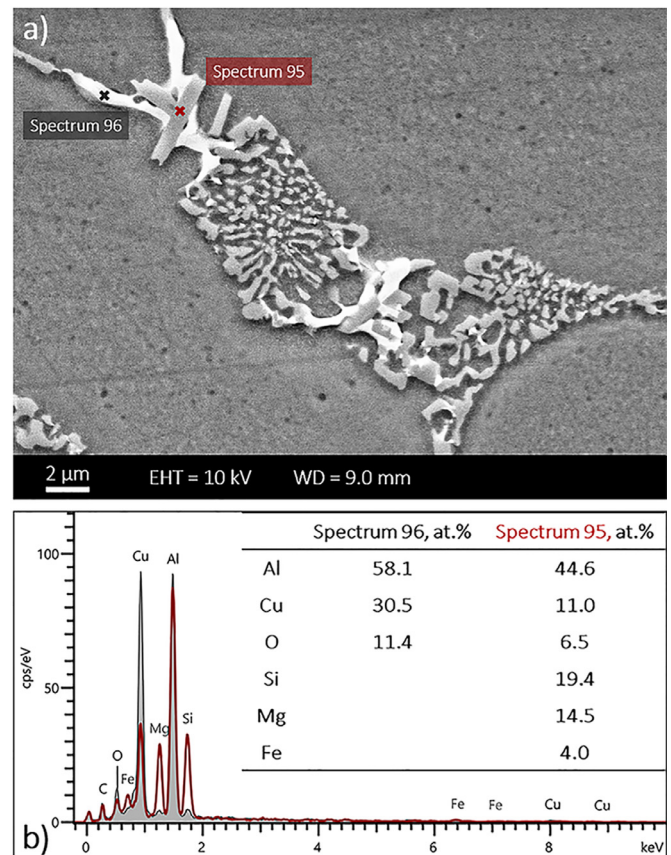
Cu concentration in the primary α-Al, and in Alloy Cu 0.5, there was a marginal difference between the centre and the edge of the dendrite.

For Alloys Cu 1.5 and Cu 3.0, the edge of the dendrites had a slightly higher Cu concentration than the centre. This concentration profile is in line with the Al-Cu phase diagram, and this became even more pronounced as the Cu content increased. For all of the alloys, the concentration of Si and Mg at the centre of the dendrite resulted in 1.47 ± 0.09 wt% and 0.03 ± 0.01 wt%, respectively. The obtained concentrations of Cu, Si, and Mg measured in the α-Al matrix agreed with previous work [14]. The microstructural investigation results for Alloys Cu 0 and Cu 0.5 showed that the presence of Mg leads to the formation of β-Mg$_2$Si and π-AlFeMgSi phases. As the Cu concentration in the alloy increased to 1.5 wt%, Mg was involved in π-AlFeMgSi, and Q-Al$_5$Mg$_8$Cu$_2$Si$_6$ phases and θ-Al$_2$Cu also formed. In Alloy Cu 3.0, the main intermetallic compounds were Q-Al$_5$Mg$_8$Cu$_2$Si$_6$ and θ-Al$_2$Cu phases. The microstructure investigation results are in agreement with the solidification sequence predicted by the Thermo-Calc simulation software for an Al-Si-Mg alloy with increasing concentration of Cu (Table 5).

The discussed intermetallic phases nucleated in the interdendritic region during eutectic solidification. SEM results obtained using EDS analyses enabled to identify Q and θ phases in Alloy Cu 3.0, as shown in Fig. 3, and confirmed that Cu was mainly involved in the Q phase in Alloys Cu 0.5 and Cu 1.5. Both phases were always found in the interdendritic region, deeply interconnected to both each other and eutectic Si.

Our observation was that the Q and θ phase appeared to be coarser than Si particles, but a specific morphology could not be assigned to either. Table 4 also presents the area fraction of Cu phases for each alloy. Calculations of the Cu content in the intermetallic compounds were according to the theoretical amount of Cu in Q-Al$_5$Mg$_8$Cu$_2$Si$_6$ (~20 wt%) and in θ-Al$_2$Cu (~54 wt%). Moreover, the results of the

Table 3
Microstructural characteristics of the alloys. Error is the standard error.

Alloy	AGS[μm]	SDAS[μm]	Si particlesED [μm]	Si particlesAspect Ratio	Si particlesArea [μm^2]	Si particlesCircularity
Cu 0	85 ± 5	8.9 ± 0.7	0.20 ± 0.09	0.57 ± 0.05	0.42 ± 0.07	0.72 ± 0.05
Cu 0.5	85 ± 5	9.0 ± 0.8	0.19 ± 0.09	0.59 ± 0.05	0.41 ± 0.07	0.74 ± 0.04
Cu 1.5	95 ± 9	9.2 ± 0.2	0.28 ± 0.09	0.58 ± 0.05	0.53 ± 0.09	0.74 ± 0.04
Cu 3.0	94 ± 10	8.8 ± 0.1	0.20 ± 0.08	0.58 ± 0.05	0.44 ± 0.07	0.72 ± 0.05

Table 4
Cu content of microstructural components. Error is the standard error.

Alloy	Primary α-Al Cu [wt%]centre	Cu [wt%]edge	Nanohardness[GPa]	Q Phase Area%	Cu [wt%]	θ Phase Area%	Cu[wt%]
Cu 0	–	–	0.66 ± 0.024	–	–	–	–
Cu 0.5	0.11 ± 0.01	0.11 ± 0.02	0.67 ± 0.015	0.5	0.11	–	–
Cu 1.5	0.37 ± 0.03	0.51 ± 0.07	0.74 ± 0.019	1.4	0.29	0.8	0.43
Cu 3.0	0.74 ± 0.04	0.90 ± 0.13	0.87 ± 0.024	2.2	0.45	2.6	1.39

Table 5
Solidification sequence of the alloys according to the Scheil simulations with Thermo-Calc.

Solidification reaction	Temperature [˚C] Cu 0.0	Cu 0.5	Cu 1.5	Cu 3.0
liq $\rightarrow$ α-Al	616	616	615	608
liq $\rightarrow$ α-Al + Si	573	572	569	565
liq $\rightarrow$ α-Al + Si + Al$_5$FeSi	566	561	558	551
liq $\rightarrow$ α-Al + Si + Al$_5$FeSi + Al$_8$FeMg$_3$Si$_6$	559	551	528	–
liq $\rightarrow$ α-Al + Si + Al$_8$FeMg$_3$Si$_6$ + β-Mg$_2$Si	557	545	–	–
liq $\rightarrow$ α-Al + Si + Al$_8$FeMg$_3$Si$_6$ + β-Mg$_2$Si + Q-Al$_5$Cu$_2$Mg$_8$Si$_6$	–	530	–	–
liq $\rightarrow$ α-Al + Si + Al$_8$FeMg$_3$Si$_6$ + Q-Al$_5$Cu$_2$Mg$_8$Si$_6$	–	–	525	–
liq $\rightarrow$ α-Al + Si + Al$_8$FeMg$_3$Si$_6$ + Al$_5$FeSi + Q-Al$_5$Cu$_2$Mg$_8$Si$_6$	–	520	518	–
liq $\rightarrow$ α-Al + Si + Al$_5$FeSi + Q-Al$_5$Cu$_2$Mg$_8$Si$_6$	–	–	–	513
liq $\rightarrow$ α-Al + Si + θ-Al$_2$Cu + Al$_5$FeSi + Q-Al$_5$Cu$_2$Mg$_8$Si$_6$	–	510	510	510

Table 6
Mechanical properties of the alloys. Error is the standard error.

Alloy	YS [MPa]	Δ_{YS}	UTS [MPa]	Δ_{UTS}	E [%]	Δ_E
Cu 0	107 ± 0.3		255 ± 0.2		19 ± 0.3	
Cu 0.5	117 ± 0.3	+ 9%	281 ± 2.5	+ 10%	15 ± 2.2	– 21%
Cu 1.5	136 ± 0.1	+ 27%	317 ± 1.0	+ 24%	14 ± 0.4	– 26%
Cu 3.0	149 ± 0.2	+ 39%	252 ± 9.0	– 1.2%	2 ± 0.3	– 90%

Table 7
Number of cycles for each tested sample.

Alloy and sample	Number of cycles
Alloy Cu 0 - sample 1	732
Alloy Cu 0 - sample 2	430
Alloy Cu 0 - sample 3	2100
Alloy Cu 0.5 - sample 1	325
Alloy Cu 0.5 - sample 2	943
Alloy Cu 1.5 - sample 1	633
Alloy Cu 1.5 - sample 2	882
Alloy Cu 3.0 - sample 1	725
Alloy Cu 3.0 - sample 2	2100

measured area fractions are in Table 4. The result was in line with the WDS measurements for the Cu concentration in the primary α-Al matrix.

The tensile properties listed in Table 6 agree with literature results: elongation continuously decreased, while YS increased with higher Cu content.

The percentage increase of YS was comparable to the results reported by Seifeddine et al. [6], who investigated alloys with chemical compositions, modification treatments, and solidification conditions similar to those described in the present work. Moreover, a drop in UTS occurs for samples with a Cu content of 3.2 wt%, whereas other authors reported this drop at lower Cu contents of around 1.5–2 wt% [3–7]. The increased quantity of Q and θ phases in Alloy Cu 3.0 was responsible for this significant drop in UTS and elongation, as highlighted by the analysis of fracture profiles and surfaces (Fig. 4).

In Alloy Cu 0, the fracture followed the eutectic regions and had a nonlinear crack profile (Fig. 4a). However, in Alloy Cu 3.0 (Fig. 4b), a significant change in crack propagation was observed. Fractured Cu phases are evident below and on the crack profile in Fig. 4b, indicating that these phases influenced the fracture propagation and affected the elongation of the alloy. Moreover, the fracture surfaces of Alloys Cu 0 (Fig. 4c) and Cu 3.0 (Fig. 4d) did not show apparent porosity. The

discrepancy between the density measurements and the theoretical density of the alloys (Table 1) highlights the presence of some porosity. However, no dependency between the Cu concentration and porosity occurs in these alloys because the material is well-fed during the directional solidification. The presence of Cu leads to intermetallic compounds and not detrimental porosities, as confirmed by the density measurements in Table 1.
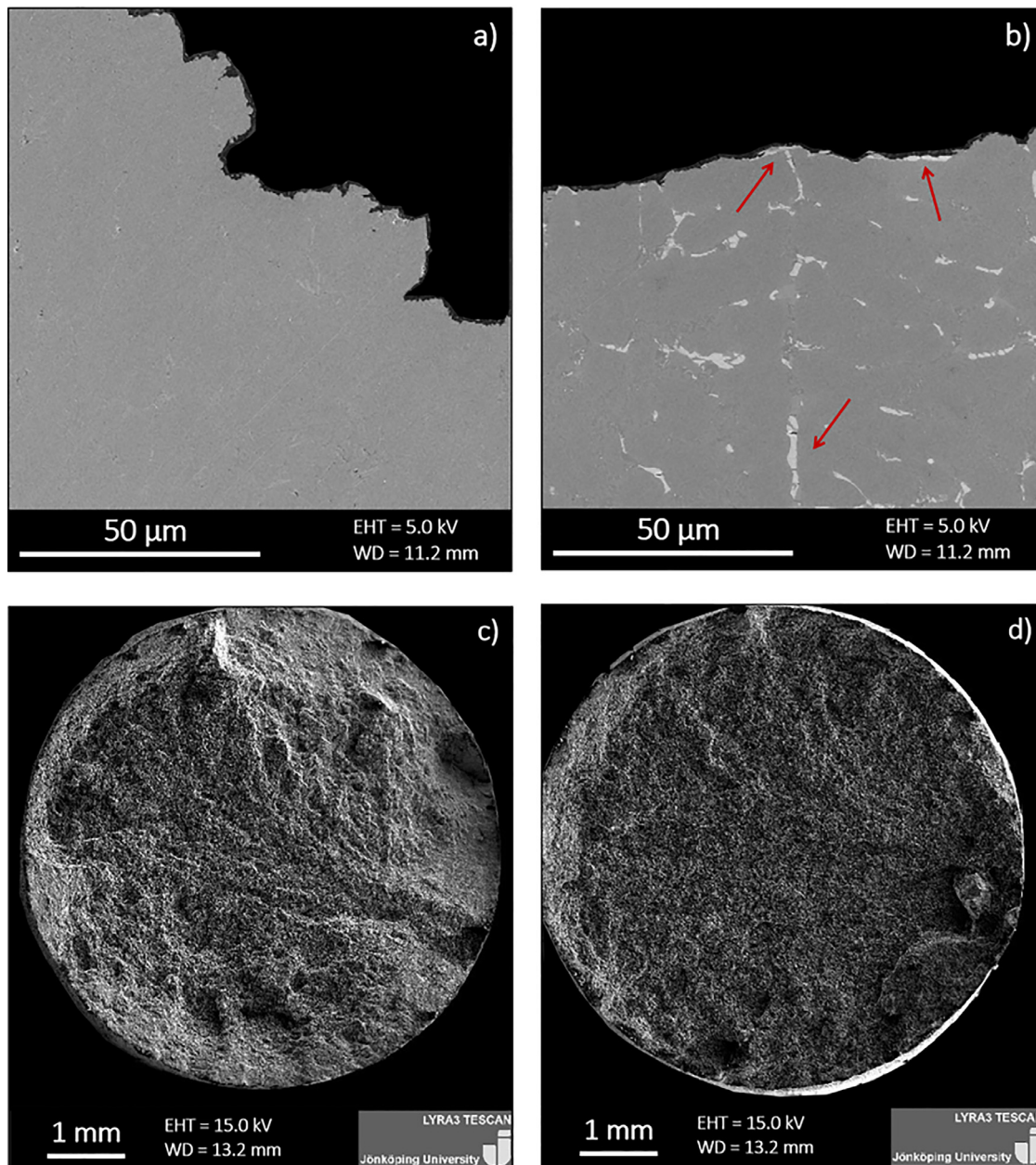
3.2. In-situ cyclic testing

Table 7 shows the number of cycles for the *in-situ* cyclic testing and all the alloys fall in the range of 325–2100 cycles. These results lie in the low cycle fatigue regime.

3.2.1. Crack initiation

The fatigue crack initiation in hypoeutectic Al–Si casting alloys usually results from defects at the surface and subsurface levels. However,

Fig. 4. Tensile fracture profiles and fracture surfaces: a, c) Alloy Cu 0; b, d) Alloy Cu 3.0. Red arrows point at fractured Cu-bearing phases, both on the fracture profile and far from it.

with a limited amount of defects, crack initiation nucleates generally from discontinuities such as slip bands, particle debonding/breakage, or grain boundaries [15,16]. Crack initiation in the investigated samples varied depending on the Cu concentration. Preloading did not result in any evident deformation, whereas during cyclic loading, fracture initiation became visible. In Alloys Cu 0 and Cu 0.5, slip bands acted as initiation sites. Moreover, in connection with the slip bands, cracking and debonding of Si particles and intermetallics took place, as depicted in the inset of Fig. 5a.

However, in alloys with 1.5 wt% of Cu content or more, slip bands were not evident as in the other alloys, and fracture nucleated either from the eutectic regions or Cu phases. An example of nucleation in the eutectic region of Alloy Cu 3.0 is depicted in the inset of Fig. 5b. This change of the nucleation behaviour is linked to the strengthening of the primary α-Al matrix as Cu increases, and crack

nucleation moves to the brittle secondary phases in the interdendritic region.

3.2.2. Crack propagation

Fatigue cracks are expected to take the path of least resistance, which is generally offered by the most damaged microstructural feature in their path.

EBSD orientation maps, acquired to detect grain boundaries before and after failure, showed that crack propagation occurred along transgranular paths in all of the investigated alloys (Fig. 6). In all cases, crack propagation in the FOV was trans-dendritic and crossed the primary α-Al matrix. Fig. 6 also depicts that the DIC analysis at 170 N loading enabled to highlight the high-strain (Von mises equivalent strain) regions in alloys with the Cu content up to 1.5 wt%. In most cases, those regions accord well with the crack path of the following cycles. On the contrary,
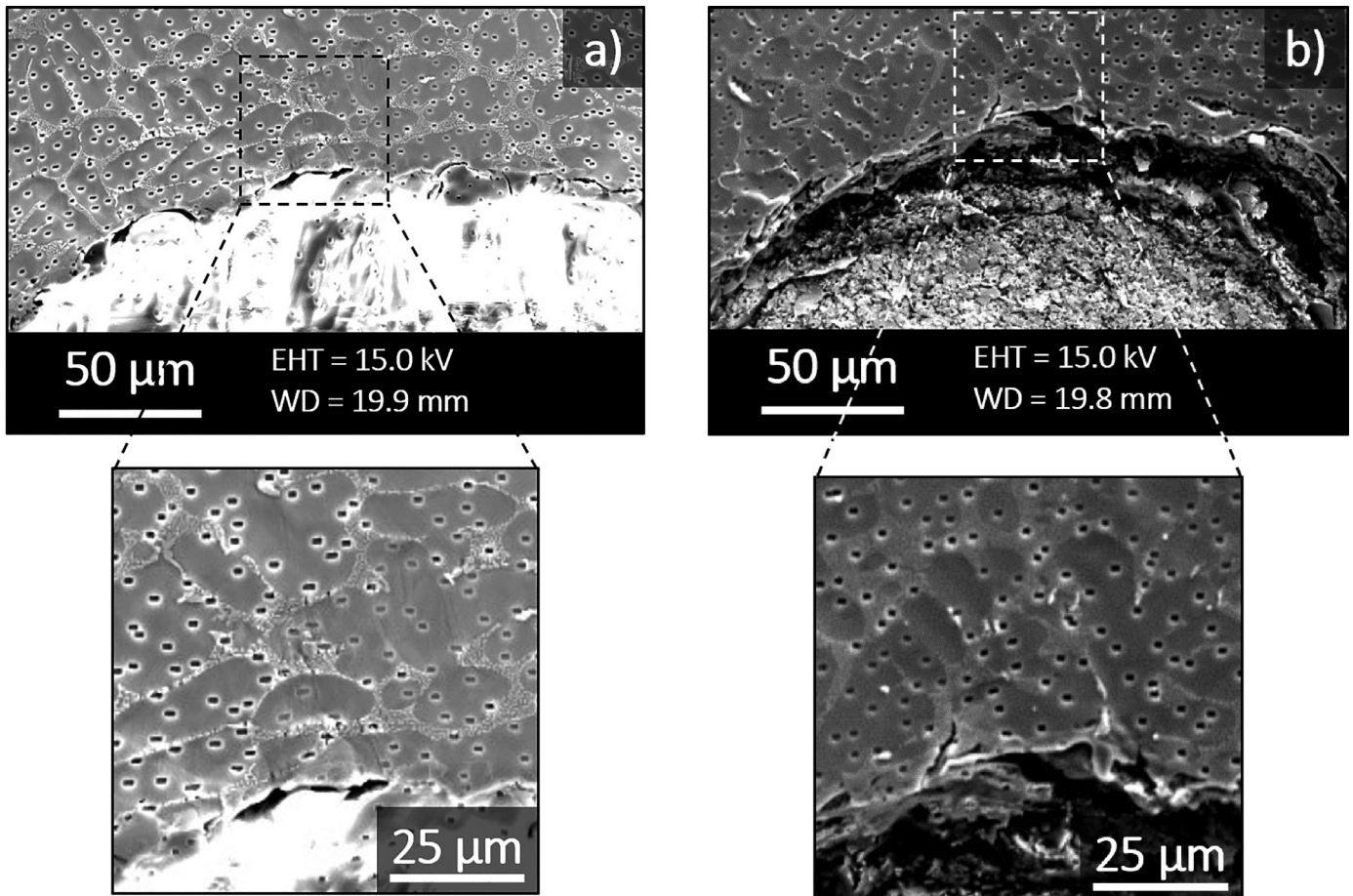
Fig. 5. Beginning of crack initiation: a) Alloy Cu 0; b) Alloy Cu 3.0.
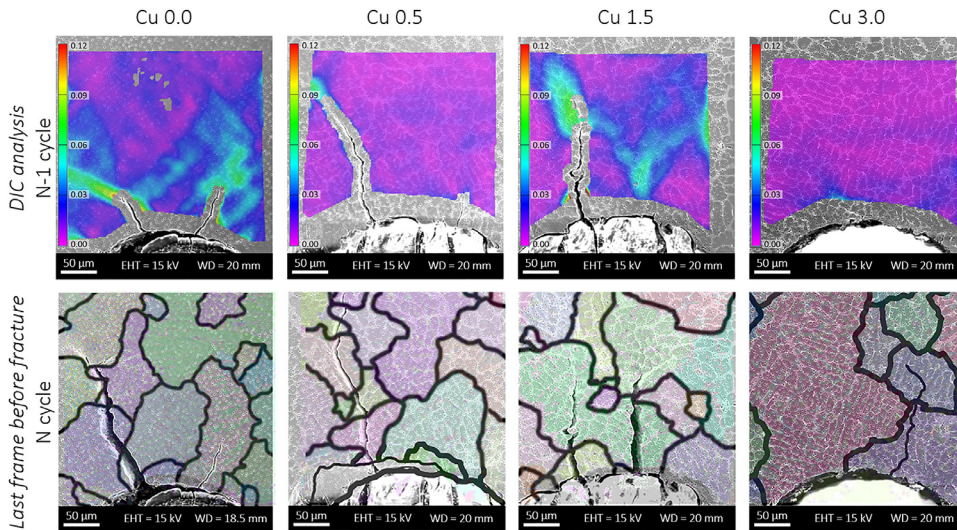

Fig. 6. Crack propagation in all alloys combining DIC and EBSD, presenting the Von mises equivalent strain concentration at N-1 cycle, and the last frame before fracture.

in Alloy Cu 3.0 strain was not detected in the FOV before the occurrence of final failure. The fracture path for the first 150 μm in alloy Cu 3.0 were taken from the final fracture and manually drawn on the picture.

In some other cases, reported in Fig. 7 as an example, the results of the DIC analysis show that the highest strain concentration occurred at the grain boundary. Nonetheless, the crack did not follow that path, and instead propagated across the dendrite arms. In other cases, a local strain concentration in the centre of the grain was evident as a result of

DIC, and cracks did not occur nearby (Fig. 7a); later, a crack appeared, most likely coming from the subsurface area (Fig. 7b). The DIC can highlight the areas affected by the highest strain in the FOV, but the crack paths do not necessarily correspond to those areas.

What is significantly affected by the presence of Cu is the response of the primary matrix. Fig. 8a and b show that in Alloy Cu 0, evident slip bands formed in the dendrite arms throughout the FOV, surrounding the propagating crack during the cyclic test. On the other hand, in
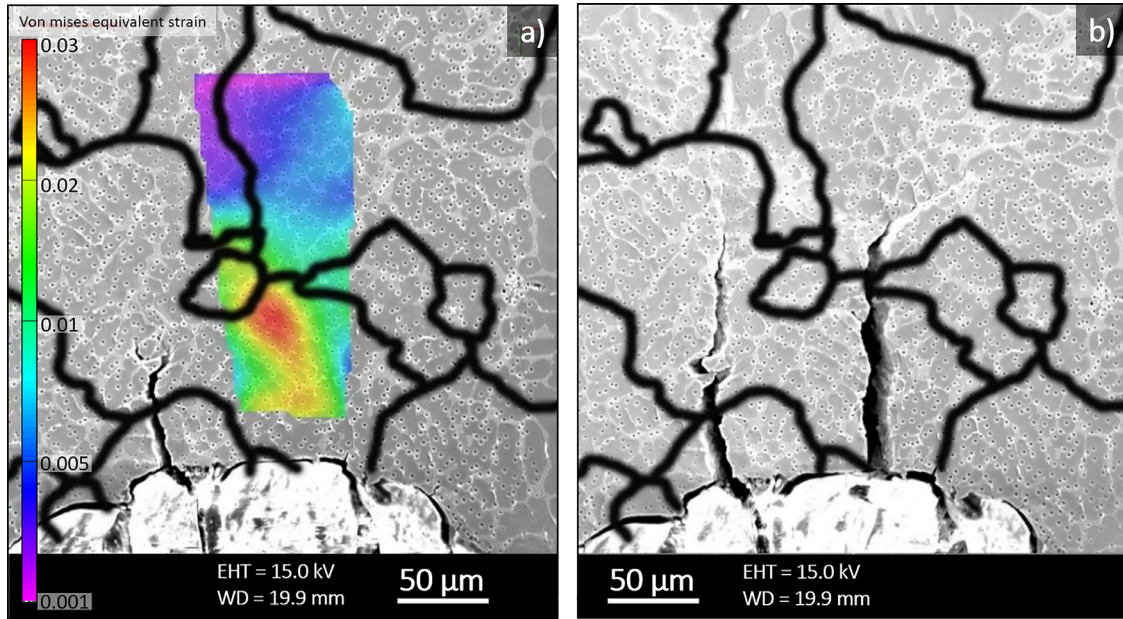
Fig. 7. Alloy Cu 1.5. a) After 600 cycles, a high strain area is visible in the area where the crack later propagated; b) After 630 cycles, following crack propagation. The superimposed black lines represent grain boundaries, obtained from EBSD maps.
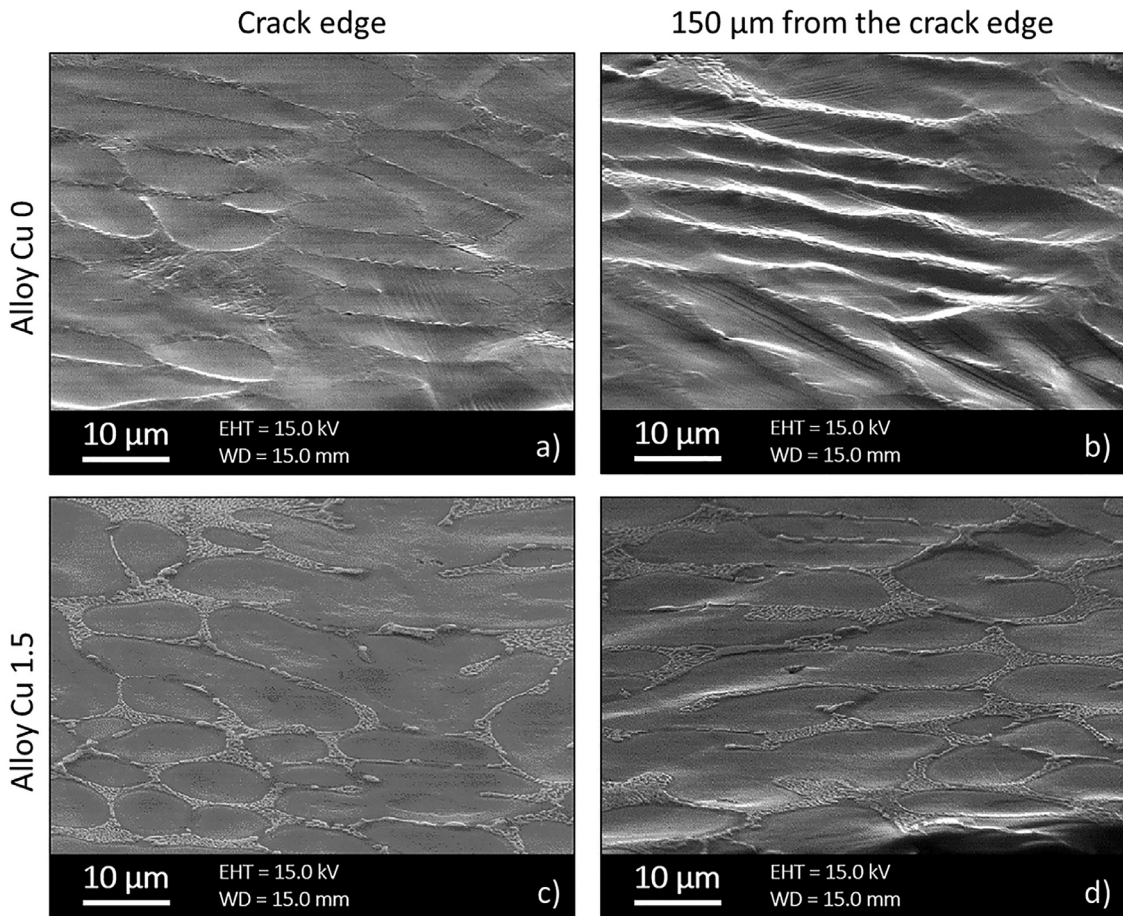

Fig. 8. Development of slip bands during the cycling testing of alloys with different Cu contents: a-b) alloy Cu 0; c-d) alloy Cu 1.5.
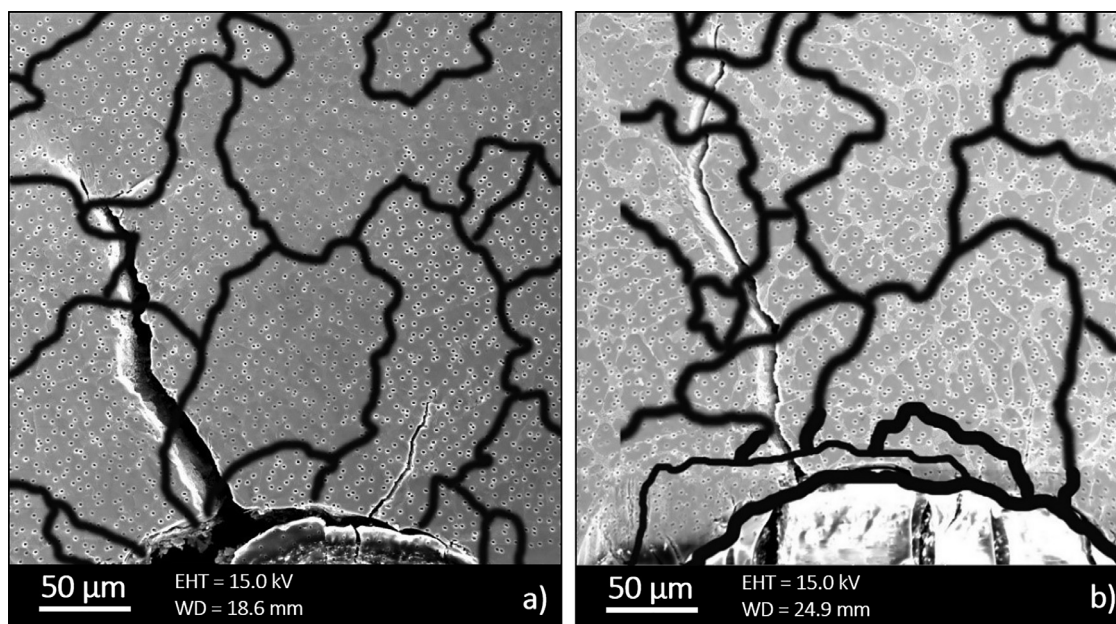
Fig. 9. Clear trans-granular crack paths in a) Alloy Cu 0; b) Alloy Cu 0.5. The superimposed black lines represent grain boundaries, obtained from EBSD maps.

Alloy Cu 1.5 slip bands are only visible on the crack edge (Fig. 8d) but do not appear in the rest of the FOV (Fig. 8c).

Besides, the crack path becomes less linear as the Cu content increases. It can be assessed with crack tortuosity, calculated as the ratio between the measured crack length and the equivalent straight path [17]. Given the definition, its values are equal to or higher than 1. In the Alloys, Cu 0 and Cu 0.5 tortuosity is ~ 1.05, and it increases to 1.2 and 1.3 for Alloys Cu 1.5 and Cu 3.0, respectively. Thus the crack path is influenced by the strengthening of the α-Al matrix and brittle Q and θ phases ahead of the crack tip.

With increasing Cu content, the concentration of Cu in the α-Al matrix increased, as shown by WDS analyses (Table 4). This increase resulted in a strengthened α-Al matrix, as highlighted by the nano-hardness results reported in Table 4. Nevertheless, the crack propagation in all of the alloys followed the α-Al matrix rather than the eutectic regions and grain boundaries in the FOV. The results show that the increased Cu concentration in the α-Al matrix, either in solid solution or fine Cu-rich precipitates, lead to a nonlinear crack propagation path still in the α-Al matrix. In this case, brittle components such as Si particles and Cu phases were expected to behave as a preferential path for crack propagation, but this phenomenon was not observed in the FOV.

In the present study, cracks were trans-dendritic as they propagated along the centre of the dendrite or across its arms in the FOV. Moreover, under these conditions, the Cu phases did not affect crack propagation. As a clarifying example of trans-dendritic and trans-granular fracture, Fig. 9 shows the crack propagation path and grain boundaries for Alloys Cu 0 (Fig. 9a) and Cu 0.5 (Fig. 9b).

Although Cu phases and Si particles are often cracked and debonded from the matrix, they did not interfere with crack paths. The hardness of eutectic Si is 11.13 ± 0.1 GPa, while that of Q and θ phases is 6.51 ± 1.5 GPa and 5.77 ± 0.7 GPa, respectively, as reported in the literature [18]. The hardness of the α-Al matrix varied from 0.66 to 0.86 GPa (Table 4), and crack propagation still occurred in the dendrites despite the increase in hardness with increasing Cu content in the α-Al matrix. A rapid failure occurred in Alloy Cu 3.0 without any previously detectable deformation, so information regarding the crack propagation in the cyclic tests is not available. The increased strength of the α-Al matrix combined with a higher quantity of Cu-rich

phases (Table 4) is the reason for the rapid failure. This behaviour is similar to that observed in tensile tests of Alloy Cu 3.0, where a sudden drop in UTS occurred despite the increase in YS. Cyclic tests highlighted that the strengthening of the matrix due to Cu plays a fundamental role in crack nucleation and propagation. The brittle compounds, expected to have a primary role in influencing the fracture behaviour of the alloy, do not have an evident effect up to 1.5 wt% Cu when the primary α-Al is the constituent that determines the overall response.

3.3. Fracture surface analyses

The investigation of the fracture surfaces of Alloy Cu 0 (Fig. 10a) revealed the starting point of the fatigue crack to be at the notch. The enlarged picture of the notch tip (Fig. 10a) shows a surface that appears regular and smooth, with some linear features identified as propagation rivers. These converged at the initiation site and delineated the fatigue propagation zone with a radius of roughly 200 μm. Fig. 11a depicts a magnification of the propagation region in Alloy Cu 0.5 that confirm flattening of the contacting areas during propagation. The remaining crack surface was irregular, characterised by tear ridges and shear elongated dimples (Fig. 11b) that are a result of local deformation, and areas of eutectic. This irregular surface corresponds to the final failure zone.

Similar results were found on the surfaces of Alloys Cu 0.5 (Fig. 10b) and Cu 1.5 (Fig. 10c), although the initiation point and the fatigue zone became less evident for these alloys than for Alloy Cu 0. Hence, a clear distinction separating the fatigue zone and the final fracture zone was possible in the alloys with Cu up to 1.5 wt%. The cracks nucleated from the notch in a region close to the polished surface, and no other starting points were evident on the fracture surface.

On the contrary, Alloy Cu 3.0 (Fig. 10d) did not display a fracture behaviour similar to the other alloys. For this alloy, the failure occurred rapidly, and the entire fracture surface showed the characteristics of a final fracture zone. A fatigue propagation zone at the notch is not present, and this clarifies that the sudden crack observed in Fig. 6 was not propagating from the sub-surface area. Moreover, the area close to the notch along the thickness revealed cleavage facets and secondary cracks, visible in Fig. 11c. These areas show a different morphology
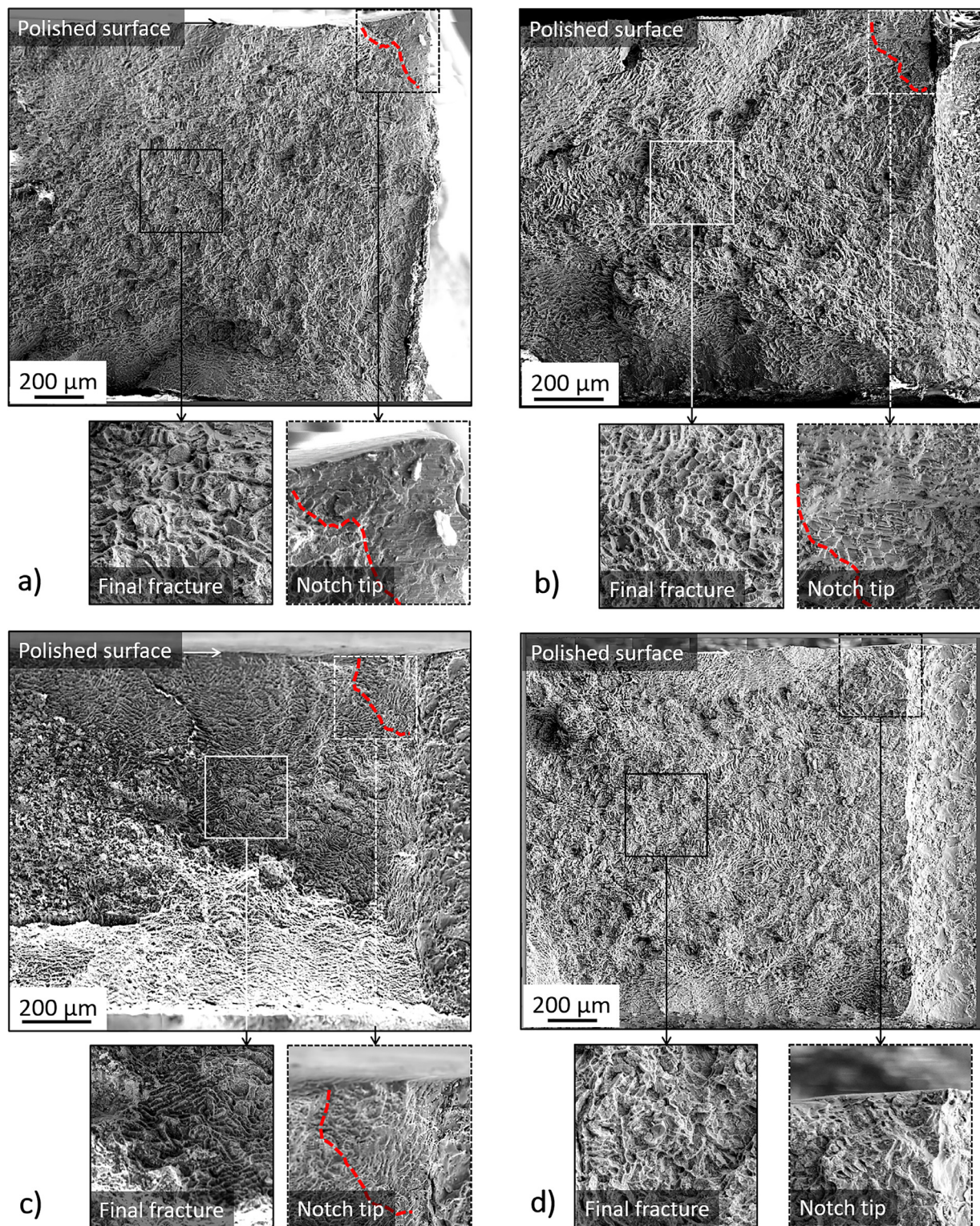
Fig. 10. Fatigue fracture surfaces. a) Alloy Cu 0; b) Alloy Cu 0.5; c) Alloy Cu 1.5; d) Alloy Cu 3.0. Dashed red lines highlight the crack initiation areas.

than the propagation areas identified in the other alloys (Fig. 11a). The alloy Cu 3.0 exhibits locally brittleness that is related to debonding of secondary phases, similar to what observed in Fig. 5b. Further away from the notch in the final fracture zone, the fracture surface showed a mixed brittle-plastic area with steep steps, tear ridges, eutectic area, Cu rich intermetallics and elongated shear dimples (Fig. 11d). The fracture surface of the alloy Cu 3.0 shows a significant increase in the brittle area of eutectic and Cu phases comparing with the Alloy Cu 0.5.

The strengthened primary matrix in Alloy Cu 3.0 and increased concentration of Q and θ phases determines the different fracture behaviour, with suppressed fatigue propagation and resulting in an almost static failure.
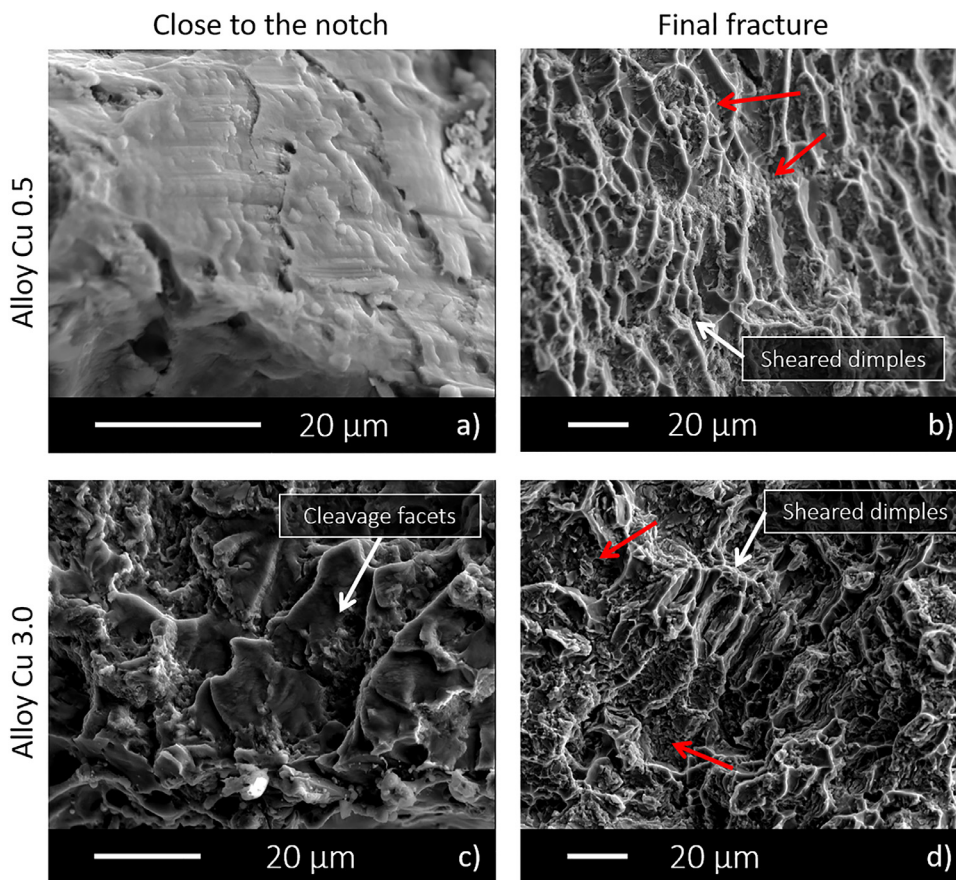
Close to the notch

Final fracture

Fig. 11. Details of fracture surfaces close to the notch (left column) and far from the notch (right column): a-b) alloy Cu 0.5; c-d) alloy Cu 3.0. Red arrows point the interdendritic regions.

4. Conclusions

The present study aimed to describe how specific microstructural features combined with the addition of Cu, are influencing the microstructure, mechanical properties, and fatigue crack nucleation and propagation of an AlSi7Mg alloy.

The increase of Cu content from 0 wt% to 3.2 wt% increased the concentration of Cu in the α-Al matrix to 0.74 wt%. Moreover, the Q-Al$_5$Mg$_8$Cu$_2$Si$_6$ and θ-Al$_2$Cu phases in Alloy Cu 3.0 covered an area fraction of 4.8%. Concerning mechanical properties, an increase in YS of 39% was achieved with the addition of 3.2 wt% Cu. Moreover, the addition of 1.5 wt% Cu increased the UTS by 24%. There was, however, a notable reduction of elongation (90%) in Alloy Cu 3.0. The directional solidification did not increase the porosity of the fracture surfaces, proving that the Cu phases are the features that significantly affect elongation.

In-situ cyclic testing coupled with DIC analysis highlight that the main effect related to Cu addition is the strengthening of the α-Al matrix due to the solid solution. This phenomenon significantly changed the alloys response to fatigue deformation. In alloys of up to 0.5 wt% Cu content, slip bands acted as initiation sites; above 1.5 wt% Cu, initiation occurred in the eutectic or intermetallic regions.

The fatigue crack paths remained trans-granular and trans-dendritic for a Cu content of up to 3.2 wt%. The primary α-Al matrix became less prone to deformation, and crack propagation changed to almost static failure in Alloy Cu 3.0, with a fracture surface that showed the characteristics of a final fracture zone. Given the critical role played by the primary α-Al, it is essential to comprehensively investigate the fracture behaviour after heat treatment in these alloys.

Declaration of Competing Interest

The authors declare that they have no known competing financial interests or personal relationships that could have appeared to influence the work reported in this paper.

Funding

References

[1] F.J. Feikus, Optimisation of Al-Si cast alloys for cylinder head applications, AFS Trans. 98–61 (1998) 225–231.

[2] L. Heusler, F.J. Feikus, M.O. Otte, Alloy and casting process optimisation for engine block application, AFS Trans. 50 (2001) 215–223.

[3] A.R. Farkoosh, M. Pekguleryuz, Enhanced mechanical properties of an Al-Si-Cu-Mg alloy at 300 C: effects of Mg and the Q-precipitate phase, Mater. Sci. Eng. A 621 (2015) 277–286.

[4] R. Taghiabadi, A. Fayegh, A. Pakbin, M. Nazari, M.H. Ghoncheh, Quality index and hot tearing susceptibility of Al-7Si-0.35Mg-xCu alloys, Trans, Nonferrous Met. Soc. China 28 (2018) 1275–1286.

[5] S.G. Shabestari, H. Moemeni, Effect of copper and solidification conditions on the microstructure and mechanical properties of Al-Si-Mg alloys, J. Mater. Process. Technol. 153–154 (2004) 193–198.

[6] S. Seifeddine, E. Sjölander, T. Bogdanoff, On the role of copper and cooling rates on the microstructure, defect formations and mechanical properties of Al-Si-Mg alloys, Mater. Sci. Appl. 4 (2013) 171–178.

[7] M.T. Di Giovanni, E. Cerri, T. Saito, S. Akhtar, P. Åsholt, Y. Li, M. Di Sabatino, How slight solidification rate variations within cast plate affect mechanical response: a study on as-cast A356 alloy with Cu additions, Adv. Mater. Sci. Eng. (2018) 4030689.

[8] C.H. Caceres, M.B. Djurdjevic, T.J. Stockwell, J.H. Sokolowski, The effect of Cu content on the level of microporosity in Al-Si-Cu-Mg casting alloys, Scr. Mater. 40–5 (1999) 631–637.

[9] M. Ma, J. Zhang, D. Yi, B. Wang, Investigation of high-cycle fatigue and fatigue crack propagation characteristic in 5083-O aluminum alloy, Int. J. Fatigue 126 (2019) 357–368.

[10] P. Huter, P. Renhart, S. Oberfrank, M. Schwab, F. Grün, B. Strauder, High- and low-cycle fatigue influence of silicon, copper, strontium and iron on hypo-eutectic Al-Si-Cu and Al-Si-Mg cast alloys used in cylinder heads, Int. J. Fatigue 82 (2016) 588–601.

[11] A.G. Spangenberger, X. Chen, D.A. Lados, Processing parameter control of lifetime-limiting failure mechanisms in Al-Si cast alloys at room and elevated temperatures, Metall. Mater. Trans. B 49B (2018) 2133–2144.

[12] K.A. Kasvayee, E. Ghassemali, K. Salomonsson, S. Sujakhu, S. Castagne, A.E.W. Jarfors, Microstructural strain mapping during in-situ cyclic testing of ductile iron, Mater. Charact. 140 (2018) 333–339.

[13] A.M. Samuel, F.H. Samuel, Effect of alloying elements and dendrite arm spacing on the microstructure and hardness of an Al-Si-Cu-Mg-Fe-Mn (380) aluminium die-casting alloy, J. Mater. Sci. 30 (1995) 1698–1708.

[14] E. Sjölander, S. Seifeddine, Optimisation of solution treatment of cast Al-7Si-0.3Mg and Al-8Si-3Cu-0.5Mg alloys, Metall, Mater. Trans. A 45A (2014) 1916–1927.

[15] L. Ceschini, A. Morri, S. Toschi, S. Seifeddine, Room and high temperature fatigue behaviour of the A354 and C355 (Al-Si-Cu-Mg) alloys: role of microstructure and heat treatment, Mat. Sci. Eng. A 653 (2016) 129–138.

[16] K. Gall, N. Yang, M. Horstemeyer, D.L. McDowell, J. Fan, The debonding and fracture of Si particles during the fatigue of a cast Al-Si alloy, Metall. Mater. Trans. A 30A (1999) 3079–3088.

[17] J. Song, C. Huang, H. Chuang, Microstructural characteristics and vibration fracture properties of Sn-Ag-Cu-TM (TM= Co, Ni, and Zn) alloys, J. Electron. Mater. 35 (2006) 2154–2163.

[18] C.L. Chen, A. Richter, R.C. Thomson, Investigation of mechanical properties of intermetallic phases in multi-component Al-Si alloys using hot-stage nanoindentation, Intermetallics 18 (2010) 499–508.